



Enhancing ROS generation and suppressing toxic intermediate production in photocatalytic NO oxidation on O/Ba co-functionalized amorphous carbon nitride



Wen Cui^a, Jieyuan Li^b, Yanjuan Sun^a, Hong Wang^a, Guangming Jiang^a, S.C. Lee^c, Fan Dong^{a,*}

^a Chongqing Key Laboratory of Catalysis and New Environmental Materials, College of Environment and Resources, Chongqing Technology and Business University, Chongqing 400067, China

^b College of Architecture and Environment, Sichuan University, Sichuan 610065, China

^c Department of Civil and Environmental Engineering, The Hong Kong Polytechnic University, Hong Kong, China

ARTICLE INFO

Keywords:

Carbon nitride
O/Ba co-functionalization
ROS
Photocatalytic NO oxidation
Toxic intermediate

ABSTRACT

The generation of toxic intermediates during the photocatalytic reaction can result in the accumulation of secondary pollutants and lead to decreased performance. Here, we first designed an O/Ba co-functionalized amorphous carbon nitride (labeled as O-ACN-Ba) by conducting targeted density functional theory calculations for short-range and directional charge transfer in electronic transportation channels. Also, the O-ACN-Ba is synthesized via a one-step *in situ* co-pyrolysis of urea and BaCO₃. The unique electronic structure O-ACN-Ba enables highly enhanced photocatalytic NO removal rate and suppresses the generation of toxic intermediate (NO₂). The O and Ba are co-functionalized as a surface electronic trapping adjuster and an interlayer electronic trapping mediator to induce the convergence and localization of intralayer-delocalized electrons. Such internal electronic structure can facilitate the adsorption and activation of NO and O₂, elongate the lifetime of photo-generated carriers, and expedite the spatial charge separation to boost significantly the generation of reactive oxygen species, thus suppressing toxic NO₂ generation. In addition, the photocatalytic NO conversion pathway on O-ACN-Ba is characterized, and an important reaction intermediate—nitrosyl species Ba-NO₈⁽⁺⁾ is discovered and found to promote the selective conversion of NO to final products (nitrites or nitrates). This work proposes a novel strategy to advance the application of photocatalytic technology for efficient and safe air purification.

1. Introduction

Environmental pollution and energy shortage have become global concerns that need to be solved by advances in cutting-edge science and technology [1–4]. Various renewable and sustainable technologies have been developed to address these challenges to date [5–7]. Among them, semiconductor-based photocatalysis has gained interdisciplinary attention as a result of its great potential to harness solar energy for degradation of typical pollutants [8–11].

Recently, some advances in photocatalytic air purification have garnered significant interest [12–15]. Nevertheless, most of the reported works have focused on the development of modification strategies to optimize photocatalytic performance, and the conversion pathway of photocatalytic pollutant oxidation as a key issue has not been clearly revealed [16]. Most importantly, the generation of possible toxic intermediates during photocatalytic reaction processes is typically neglected, despite the fact that it could result in the accumulation of

secondary pollutants and decrease the photocatalytic performance. For instance, increased production of toxic intermediate NO₂ would probably result in its release to air during photocatalytic NO removal process. In order to promote the application of photocatalytic technology in NO purification without increasing secondary pollution, the generation of NO₂ must therefore be suppressed [17]. Thus, it is necessary to explore photocatalysts with favorable electronic structures that would enhance photocatalytic efficiency and inhibit the generation of toxic intermediates simultaneously.

Generally, a semiconductor-based photocatalysis reaction involves three steps: (1) the illumination over photocatalyst to induce the formation of electrons/holes pairs; (2) the migration and transformation of photogenerated carriers to generate the reactive oxygen species (ROS); (3) the initiation of photocatalytic redox reaction by the ROS [18–22]. As a consequence, a comprehensive atomic-level design is required to realize synergistic effects in terms of visible-light utilization, charge carrier separation, and oxidation ability of radicals, with the aim to

* Corresponding author.

E-mail address: dfctbu@126.com (F. Dong).

attain optimized photocatalytic efficiency and complete pollutant mineralization [23].

Graphitic carbon nitride (labelled as CN), a metal-free layered conjugated semiconductor, has been extensively applied in the area of environmental remediation and solar energy conversion owing to its facile synthesis, appealing electronic structure, high physicochemical stability, and “earth-abundant” nature [24–27]. As a result of the polymeric character of CN, its electronic structure can be easily tailored by means of surface engineering at the atomic-level in order to enhance its photocatalytic performance [28–30]. In particular, CN is limited by the intrinsic graphitic sp^2 -hybridized array of tri-s-triazine repeating units and the inert stack of layers, which enable delocalized photo-generated electrons to transfer in planes randomly, leading thus to a high charge-recombination rate [31–33]. Therefore, the internal electronic structure of CN can be rationally designed and tailored to promote the redistribution and delocalization of electrons, to achieve elongated lifetime of photogenerated carriers and expedited spatial charge separation, and thus to accelerate generation of abundant ROS that are capable of participating in photocatalysis [34–37]. The construction of local electronic trapping/converging districts and intercalating interlayer electronic mediators simultaneously is a novel strategy that could allow the random migration of electrons in planes and weak Coulomb interactions between layers to be modulated, realizing thus efficient charge separation and localization of electrons to optimize photocatalytic efficiency.

Here, by conducting targeted density functional theory (DFT) calculations, we first propose a conceptual design for the internal electronic structure of CN. Local electronic trapping segments (labeled as ETS) and surface electronic trapping adjusters (labeled as ETA) are introduced into CN to induce the convergence and localization of delocalized intralayer electrons. Simultaneously, interlayer electronic trapping mediators (labeled as ETM) are intercalated to bridge adjacent CN layers in order to direct the transfer of photogenerated electron. Exploiting the synergistic contributions of ETS, ETA, and ETM, an O/Ba co-functionalized amorphous carbon nitride (labeled as O-ACN-Ba) with oriented electron transportation channels is designed for the first time, resulting in an exceptionally high charge-separation rate and thus enhanced ROS generation for the photocatalytic oxidation of NO into nitrites or nitrates. Subsequently, the crafted O-ACN-Ba is synthesized via a facile one-step *in situ* co-pyrolysis of urea and $BaCO_3$. The experimental and theoretical methods are highly combined to demonstrate the successful fabrication of O-ACN-Ba, elucidate the photocatalytic NO conversion pathway, and illustrate the promotion mechanisms in terms of enhanced photoelectric properties and photocatalytic efficiency. The designed photocatalyst possesses a perfect inner electronic structure that not only facilitates the adsorption and activation of gas molecules to participate in photocatalytic NO oxidation but also expedites the spatial charge separation to optimize photocatalytic efficiency through the boosted generation of ROS. The present work represents a novel strategy for simultaneously enhanced photocatalytic efficiency and inhibited generation of toxic intermediates, and provides a new method for advancing the development of photocatalytic technology for efficient and safe air purification.

2. Experimental

2.1. DFT calculations

All spin-polarized DFT-D2 calculations were performed with the “Vienna ab initio simulation package” (VASP 5.4), utilizing a generalized gradient correlation functional [38,39]. A plane-wave basis set with a cut-off energy at 450 eV within the framework of the projector-augmented wave method was used [40,41]. The Gaussian smearing width was set to 0.2 eV. The Brillouin zone was sampled with a $3 \times 3 \times 1$ K points. All atoms were converged to 0.01 eV/Å. The *ab initio* molecular dynamics (AIMD) calculations were carried out to

verify the CO_3^{2-} dissociation process at 823 K using *Born-Oppenheimer* approximation [42,43]. A $2 \times 2 \times 3$ supercell of bulk CN that includes 168 atoms was first relaxed, and subsequently Ba and CO_3^{2-} were introduced into the interlayer and intralayer, respectively (Fig. S1a and b).

The formation energy (E_f) is defined as:

$$E_f = E_{\text{modified CN}} - (E_{\text{pure CN}} + E_{\text{species}}) \quad (1)$$

where E_{species} refers to the total energy of $BaCO_3$ species, which is calculated from its unit cell.

The adsorption energy (E_{ads}) is defined as:

$$E_{\text{ads}} = E_{\text{tot}} - (E_{\text{CN}} + E_{\text{mol}}) \quad (2)$$

where E_{tot} , E_{CN} , and E_{mol} represent the total energy of the adsorption complex, the pure CN, and the isolated molecule, respectively.

2.2. Sample preparation

The O-ACN-Ba-X samples were synthesized via co-pyrolysis of urea and $BaCO_3$. At first, 10 g of urea and a known amount of $BaCO_3$ (0.015, 0.030, 0.060, and 0.100 g) were added to an alumina crucible (50 mL) with 20 mL distilled water. The obtained solution was dried in oven at 60 °C to furnish the solid precursors. The solid precursors were placed in a semi-closed alumina crucible with a cover and calcined at 550 °C for 2 h at a heating rate of 15 °C/min in static air. After the thermal treatment, the obtained samples with different weight ratios of urea and $BaCO_3$ were collected and labeled as O-ACN-Ba-X (where X represents the amount of $BaCO_3$). For comparison, an *ex situ* mechanical mixture of CN and $BaCO_3$ was prepared and named as CN-Ba. Detailed information on characterization of the catalysts is available in Supplementary Material.

2.3. In situ DRIFTS investigation

In situ DRIFTS measurements were conducted using a TENSOR II FT-IR spectrometer (Bruker) equipped with an *in situ* diffuse-reflectance cell (Harrick) and a high-temperature reaction chamber (HVC), as shown in Scheme S1. Detailed descriptions of the *in situ* DRIFTS apparatus are available in the Supplementary Material.

Before measurements, the as-prepared samples were placed in a vacuum tube and pretreated 1 h at 300 °C. The background spectra are recorded before injecting NO into the reaction chamber. And the NO absorption bands appear once NO comes in contact with the photocatalyst at 25 °C under dark conditions. Once the adsorption equilibrium is achieved, a visible-light source is applied to initiate the photocatalytic reaction. And the “baseline” spectra are the same as that of “the curve of adsorption equilibrium” in NO adsorption process. As for the temporal evolution of normalized absorbance about adsorbed species on photocatalysts surface, the integration of characteristic absorption bands of adsorbed species leads to follow their individual evolutions as a function of time. For all species, the normalized absorbance is calculated by considering their individual maximum absorbance as 1.

2.4. Visible-light photocatalytic NO removal

The photocatalytic activity was investigated by examining the removal ratio of NO at ppb levels (500 ppb) in a continuous-flow reactor (rectangular reactor, 30 cm × 15 cm × 10 cm). The concentration of NO was continuously detected by a NO_x analyzer (Thermo Environmental Instruments Inc., model 42c-TL), which can monitor the concentration of NO, NO_2 , and NO_x (NO_x represents NO + NO_2). The as-prepared sample (0.20 g) of the catalyst was dispersed and coated onto two glass dishes (12.0 cm in diameter) for photocatalytic activity tests. A 150-W commercial tungsten halogen lamp (average light

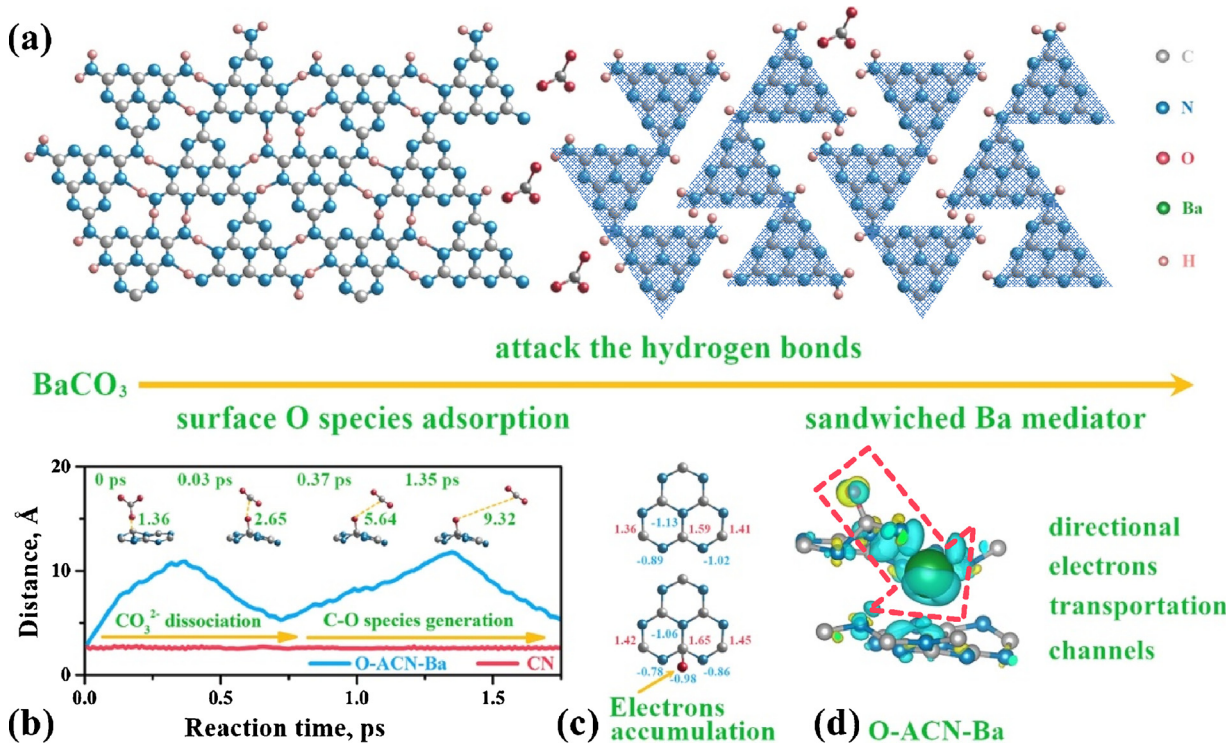


Fig. 1. The design of the O-ACN-Ba electronic structure. Top view of the atomic structure of layered carbon nitride and amorphous carbon nitride (a); time evolution in 2 ps for CO_3^{2-} dissociation at a temperature of 823 K in the course of *in situ* pyrolysis (b); Bader effective charge of CN and O-ACN-Ba (c); charge difference distribution of O-ACN-Ba (d); charge accumulation is shown in blue and depletion in yellow; isosurfaces are set to 0.005 eV \AA^{-3} . All lengths are given in \AA (For interpretation of the references to colour in this figure legend, the reader is referred to the web version of this article).

intensity = 0.16 W/cm²) was placed vertically outside and above the reactor. The lamp was turned on when the adsorption–desorption equilibrium was achieved. The removal ratio (η) of NO was calculated as $\eta = (1 - C/C_0) \times 100\%$, where C and C_0 are the concentrations of NO in the outlet steam and the feeding stream, respectively.

3. Results and discussion

3.1. Electronic structure and microstructure

The O/Ba co-functionalized amorphous carbon nitride is composed of three parts, namely ETS, ETA, and ETM, which function differently. Local electronic trapping/converging districts (including ETS and ETA) can be formed by the destruction of periodic arrangement of melon strands and surface O-adsorption, which facilitate the convergence and localization of intralayer-delocalized photogenerated electrons. Simultaneously, interlayer electronic delivery channels are constructed *via* intercalation of the Ba-mediator (ETM), realizing thus spatial charge separation. Detailed atomic-level O-ACN-Ba structure is simulated using DFT calculations and is illustrated in Fig. 1.

During the thermal polymerization process, CO_3^{2-} from BaCO_3 tends to attack the intralayer hydrogen bonds in CN and destroy the periodic arrangement of intralayer melon strands (hydrogen bonds) for constructing ETS. The process of hydrogen bond fracture can be simulated by CO_3^{2-} adsorption on CN. The exothermic nature of this process (-2.979 eV) indicates that the hydrogen bonds are broken easily by the introduction of CO_3^{2-} , which contributes to the formation of amorphous carbon nitride consisting of basic ETS units. The formation of ETS shortens the effective transmission distance required for carriers to arrive at the active site (*i.e.*, fracture point of hydrogen bonds). In other words, the long-range charge transfer in CN can be transformed to short-range charge transfer in the ETS units, reducing thus the possibility of recombination during the carrier-transfer process.

Simultaneously, CO_3^{2-} as the donor of surface O species on ETS can

result in the formation of ETA, inducing thus the convergence and localization of local intralayer electrons that transfer randomly. To test this reasoning, the dissociation process was simulated at atomic level by time evolution in 2 ps at 823 K in the course of *in situ* pyrolysis *via ab initio* molecular dynamics (AIMD) calculations. As shown in Fig. 1b, the C–O bond lengths of CO_3^{2-} fluctuate around 2.65 \AA from the start point (< 0.03 ps), and significant bond breakage of C–O is observed rapidly at < 0.4 ps. After that, a dangling CO_2 molecule shifts randomly at the boundary of crystal lattice and the left O atom is gradually bonded with the C atom to form surface O species, generating the basic ETA unit. In addition, the local charge distributions in the surface layer are visualized by the calculation of Bader effective charge (Fig. 1c) [44]. The introduction of O species gives rise to electron depletion of the adjacent C and N atoms and guides these electrons to the O atom. This behavior stems from the differences in electronegativity among the elements C, N, and O. According to the results of the DFT calculations, the CO_3^{2-} from BaCO_3 plays a crucial role not only in attacking the intralayer hydrogen bonds but also in acting as the source of surface O species, resulting therefore in the effective separation of local electrons and holes.

Differences in charge density distribution can illustrate the gain or loss of electrons, and in this work these differences were used to demonstrate the subtle role of Ba mediator (ETM) species sandwiched between adjacent layers. As shown in Fig. 1d, the intercalation of Ba mediator bridges the contiguous layers and builds an interlayer electron-delivery channel to realize interlayer charge transfer and spatial charge separation. Using targeted theoretical calculations, we designed the electronic structure of O-ACN-Ba to exploit the synergistic contribution of ETS, ETA, and ETM units. We envisaged that the designed O-ACN-Ba with localized electrons and directed charge transfer could realize the elongated lifetime of photogenerated carriers and expedited spatial charge separation. Subsequently, there are abundant electrons which activate the gas molecules on photocatalysts and thus dramatically facilitate the conversion of pollutants and the production of

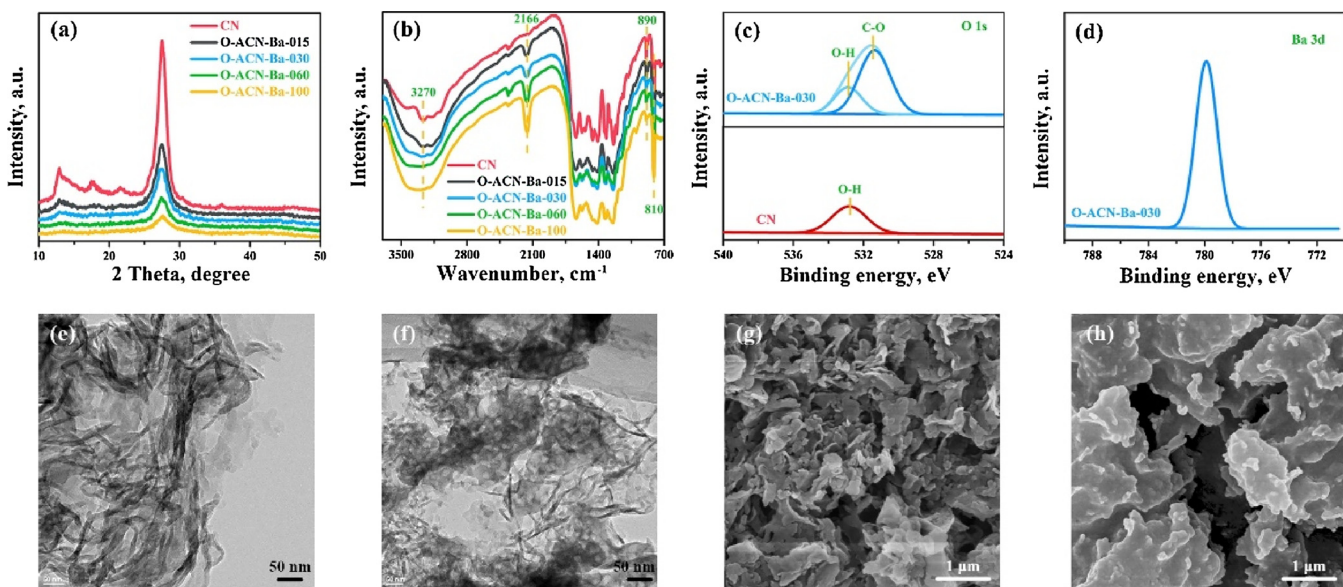


Fig. 2. Chemical composition and phase structure of the as-prepared samples. XRD patterns (a) and FT-IR spectra (b) of CN and O-ACN-Ba-X; XPS spectra (O 1s) of CN and O-ACN-Ba-030 (c); high-resolution XPS spectra (Ba 3d) of O-ACN-Ba-030 (d); TEM images of CN (e) and O-ACN-Ba-030 (f); SEM images of CN (g) and O-ACN-Ba-030 (h).

reactive species, enhancing the overall efficiency of photocatalytic NO removal.

Inspired by the theoretical design, a series of samples with O-ACN-Ba structure have been synthesized with different weight ratios of BaCO₃ to urea. The prepared samples are labeled as O-ACN-Ba-X (where X represents the content of BaCO₃). XRD analysis of CN and O-ACN-Ba-X samples (Fig. 2a) reveals two characteristic diffraction peaks of CN (13.1° and 27.2°), which arise respectively from the in-plane structural repeating motifs of the aromatic systems and the interlayer reflection of a graphite-like structure [27,45], and indicate that the graphitic-like layered structures are maintained after modification. However, two diffraction peaks characteristic of CN decreased significantly following the introduction of BaCO₃ to form nearly amorphous carbon nitride. These results suggest that the in-plane periodicity of the aromatic systems is destroyed and, correspondingly, the periodic stacking of the layers is disturbed. Subsequently, the shift of the characteristic diffraction peak of CN originating from the intercalation of Ba mediator between adjacent layers of CN is difficult to be observed because of the amorphous property of CN. As illustrated in Fig. 1a, CO₃²⁻ arising from BaCO₃ can attack the intralayer hydrogen bonds through synergic interactions between CN and BaCO₃ to form amorphous carbon nitride, resulting thus in the fabrication of ETS.

The FT-IR spectra (Fig. 2b) were measured to further verify the basic substructure units of the CN polymers (heptazine heterocyclic ring units, C₆N₇). As shown in Fig. 2b, the strong adsorption bands corresponding to the stretching vibration mode of the C₆N₇ units are observed in the spectrum of each prepared O-ACN-Ba-X sample in the 1700–1200 and 810 cm⁻¹ range [46,47], indicating thus that the O-ACN-Ba-X samples retained the basic CN atomic structure. Meanwhile, the decreased absorption band (at 3500–3100 cm⁻¹ and 890 cm⁻¹) assigned to the N–H components stemming from uncondensed amino groups are reflected, indicating the breakage of hydrogen bonds [48]. In addition, the FT-IR spectra revealed the appearance of a new absorption band at 2166 cm⁻¹, which can be associated with the stretching vibration of N=C=N (according to the Sadtler handbook of infrared spectra). These observations further demonstrate that the introduction of BaCO₃ during the urea polymerization process destroys the periodic arrangement of interlayer melon strands (hydrogen bonds), while simultaneously maintaining the basic atomic structure of CN (C₆N₇ units) to afford unique amorphous arrangements of short-range order and

long-range disorder. Therefore, through a combination of theoretical and experimental analysis, we can confirm that the CO₃²⁻ plays a vital role in the formation of ETS for facilitating the separation of carriers and exposing new active sites.

The chemical composition and valence states of the elements were examined using XPS analysis. As shown in Fig. S2a, the N1s spectra can be deconvoluted into three peaks at 398.9 eV, 400.1 eV and 401.4 eV, corresponding to the sp²-bonded N involved in the triazine rings (C=N=C), the tertiary nitrogen N-(C)₃ groups, and the amino functions (C-N-H), respectively. Besides, the corresponding binding energies of C1s at 284.8 and 288.2 eV can be ascribed to the sp²-C–C bonds and sp²-bonded carbon in the N-containing aromatic rings (N-C=N), respectively (Fig. S2b). The C=N=C, N-(C)₃, and N-C=N groups make up the basic substructure units (heptazine heterocyclic ring, C₆N₇) of CN polymers. Apparently, the concentration of O increased significantly from 1.22% in CN to 3.31% in O-ACN-Ba-030 (Fig. 2c). When compared to pure CN, the O 1s spectrum of O-ACN-Ba-030 could be deconvoluted into two peaks at 532.9 eV and 530.8 eV, which are ascribed to surface adsorbed water and adsorbed O species, respectively [49,50]. In addition, Ba is detected in the high-resolution XPS spectrum (Ba 3d) of O-ACN-Ba-030 (Fig. 2d) and the atomic ratio of barium to nitrogen (Ba : N) for O-ACN-Ba-030 is 2.1% (Table S1), which is indicative of Ba-doping in CN. Based on the results of experimental and theoretical analyses, the desired O-ACN-Ba structure containing ETS, ETA, and ETM can be readily fabricated using a facile co-pyrolysis method to facilitate the adsorption and activation of gas molecules participating in photocatalytic NO oxidation and expediting the spatial charge separation for optimized photocatalytic efficiency.

The morphologies and microstructures of CN and O-ACN-Ba-030 were examined by TEM and SEM (Fig. 2e–h). The analysis showed that the silk-like nanosheets typical of CN are well preserved after the introduction of BaCO₃. In addition, the EDX elemental mapping of O-ACN-Ba-030 (Fig. S3) suggests that the C, N, Ba, and O elements are distributed uniformly. Also, the increased concentration of Ba can be observed in EDX elemental mapping along with the introduction of the increased amount of BaCO₃. The N₂ adsorption-desorption isotherms (Fig. S4) of CN and O-ACN-Ba-X samples displayed type IV and H3 hysteresis loops, which indicates that the introduction of BaCO₃ did not influence the pore structure of CN. All relevant parameters such as specific surface area (S_{BET}) and pore volume are listed in Table S1 for all

samples. Although the specific surface area of O-ACN-Ba-X decreased following the O/Ba co-functionalization, this change had no negative effect on the photocatalytic activity of the material, as will be discussed later.

3.2. Photocatalytic mechanism and inhibition of toxic intermediates

Owing to the delicate design of the inner electronic structure, adsorption and activation of pollutants or toxic intermediates on O-ACN-Ba-based photocatalysts are expected to be elaborated. The *in situ* diffuse reflectance infrared Fourier transform spectroscopy (DRIFTS) was used to dynamically monitor the intermediates and products on the photocatalyst surface in time sequence during NO adsorption and photocatalytic NO oxidation processes.

During the NO adsorption process (the full range of *in situ* DRIFTS spectra are shown in Fig. S5a and b), absorption bands characteristic for NO appeared once NO was introduced onto the photocatalysts at 25 °C in dark conditions. This dark reaction arises from the reactive pyridine N atoms, which preferably donate its lone-pair electrons to O₂ molecules, producing active O-containing species as oxidants [51,52]. Compared to the pristine CN, a clear new band at 2129 cm⁻¹ associated with nitrosyl species (Ba-NO^{δ(+)}) over O-ACN-Ba-030 was observed in Fig. 3a, and the generation of Ba-NO^{δ(+)} was significantly boosted as suggested by the evolution of the normalized absorbance of species (Fig. 3c) [53,54]. Compared to other nitrogen-containing species, the adsorbed Ba-NO^{δ(+)}, as the main adsorption intermediate, would be preferentially oxidized to nitro compounds by ROS during the photocatalytic NO oxidation process [54,55]. Consequently, the enhanced accumulation of Ba-NO^{δ(+)} on O-ACN-Ba could minimize the possibility of toxic intermediate (NO₂) generation in the photocatalytic

oxidation process. Simultaneously, the IR adsorption bands associated with NO₂ were observed and increased in intensity in a pattern similar to that observed for the evolution of Ba-NO^{δ(+)}. Thus, the constructed O-ACN-Ba structure can facilitate the adsorption and activation of NO, giving rise to enhanced photocatalytic NO oxidation performance.

Subsequently, we recorded the time-dependent IR spectra of CN and O-ACN-Ba-030 under visible-light irradiation in time sequence once the adsorption equilibrium achieved (the full range of *in situ* DRIFTS spectra is shown in Fig. S5c and d). As shown in Fig. 3d, higher quantity of final products (NO₃⁻) was generated on O-ACN-Ba than on pristine CN. Most importantly, comparing the normalized absorbance of NO₂ evolution (Fig. 3c, f), the quantity generated of NO₂ for O-ACN-Ba-030 sample was much higher than for pure CN during the NO adsorption process. However, the accumulated NO₂ was consumed noticeably during the course of the photocatalytic NO oxidation reaction, indicating that the adsorbed NO₂ can be transformed into nitrites or nitrates more effectively than that in CN. Therefore, the unique electronic structure of O-ACN-Ba can dramatically promote the adsorption and activation of pollutants, inhibit the accumulation of harmful intermediates, and enhance the photocatalytic NO removal efficiency.

The full range of *in situ* DRIFTS spectra and the corresponding discussion on the conversion pathways underlying the photocatalytic NO oxidation over CN and O-ACN-Ba-030 are provided in the Supplementary Material.

3.3. ROS generation and photocatalytic NO purification

To better understand the mechanism of NO adsorption on O-ACN-Ba, the NO activation was probed using DFT calculations. As shown in Fig. 4a, more marked electron depletion was observed for NO on the O-

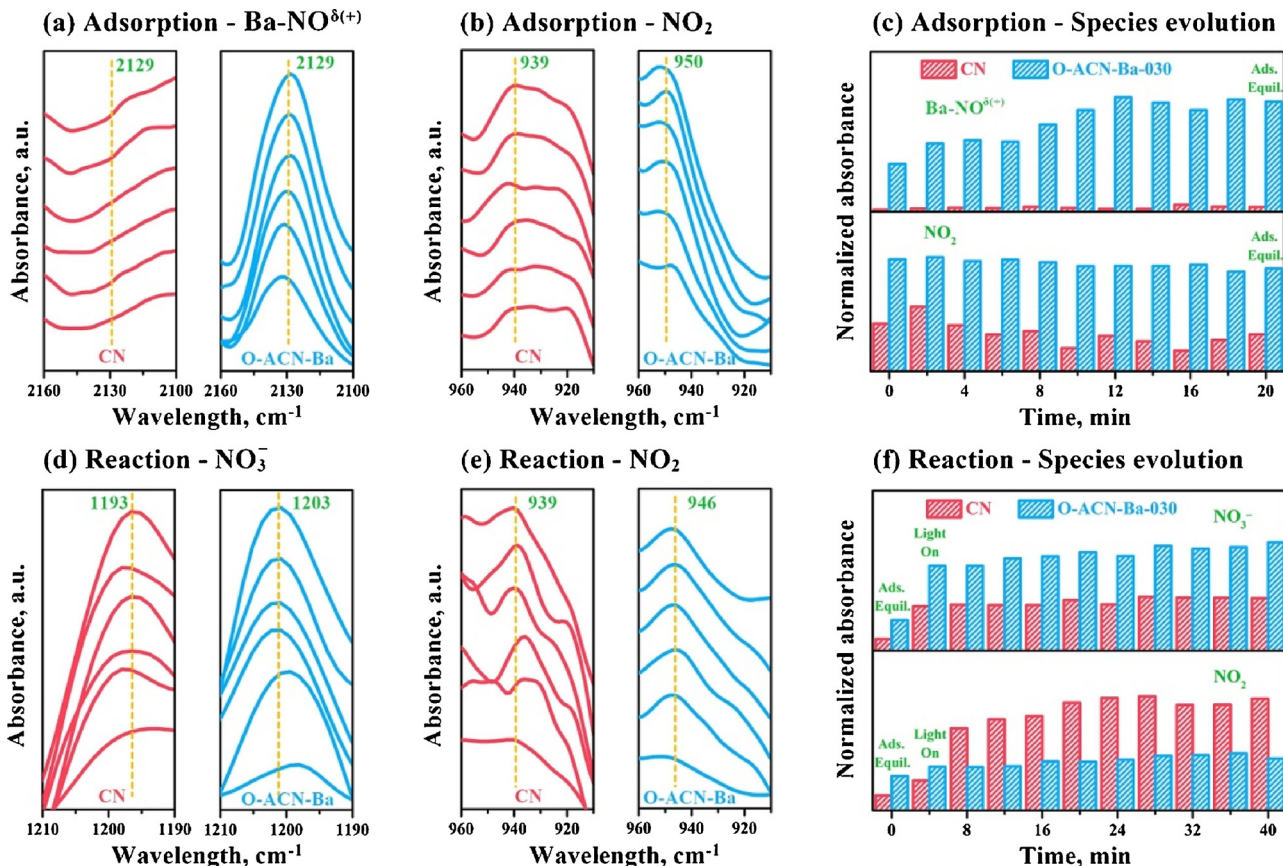


Fig. 3. *In situ* DRIFTS spectra of NO adsorption and reaction: local *in situ* DRIFTS spectra (a, b) and changes in normalized absorbance of species (c) on CN and O-ACN-Ba-030 surface during NO adsorption process (Ba-NO^{δ(+)}) and NO₂); local *in situ* DRIFTS spectra (d, e) and changes in normalized absorbance of species (f) on CN and O-ACN-Ba-030 surface during visible-light photocatalytic reaction process (NO₃⁻ and NO₂).

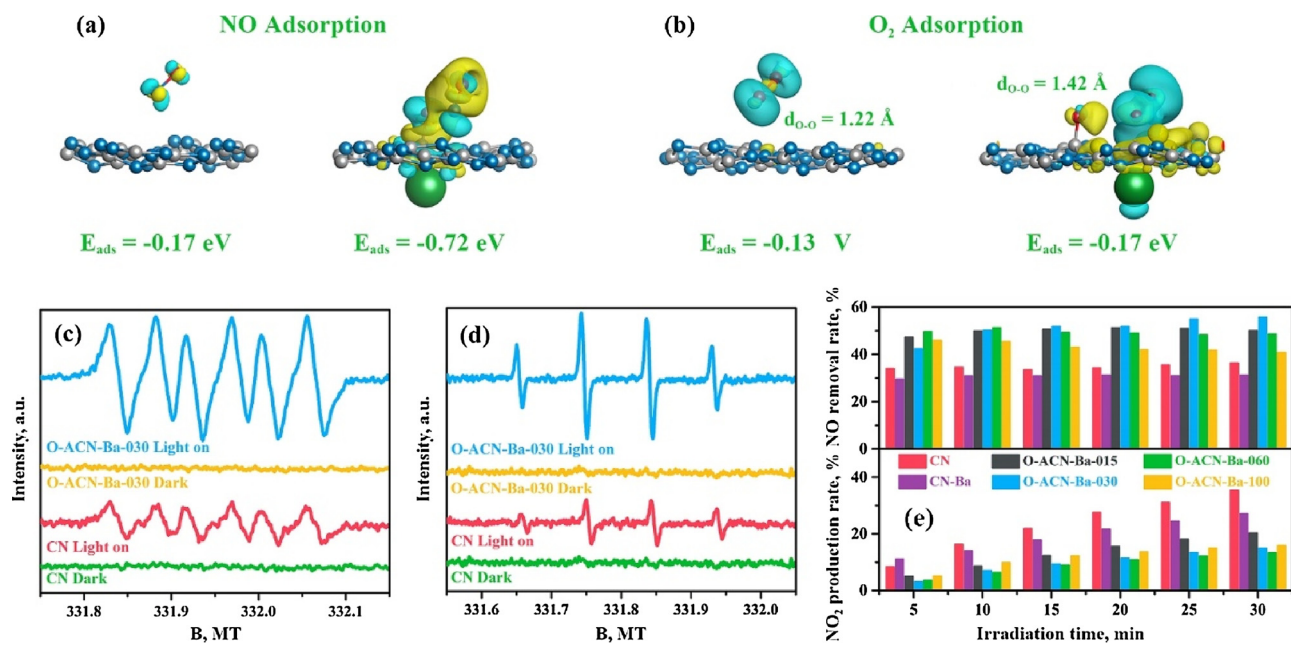


Fig. 4. Adsorption and activation of gas molecules and photocatalytic activity. Calculated differences in charge density distributions for NO (a) and O₂ (b) activation on pristine CN and O-ACN-Ba: charge accumulation is shown in blue and depletion in yellow; the isosurfaces are set to 0.005 eV Å⁻³; all lengths are given in Å; E_{ads} stand for the adsorption energy of adsorption molecule, negative values indicate heat release and charge obtainment; gray, blue, green, red and pink spheres stand for C, N, Ba, O and H atoms, respectively; DMPO ESR spectra in darkness and under visible-light ($\lambda \geq 420$ nm) irradiation for 15 min, respectively in methanol dispersion for ·O₂⁻ (c) and in aqueous dispersion for ·OH (d); NO removal efficiency and NO₂ production rate of the as-prepared samples during visible-light photocatalytic reaction process (e) (For interpretation of the references to colour in this figure legend, the reader is referred to the web version of this article).

ACN-Ba structure than on CN, indicating that the NO adsorption on O-ACN-Ba is facilitated *via* donation of electrons to electron-deficient areas in O-ACN-Ba. This process, in turn, leads to an increase in adsorption energy (from -0.165 eV for pristine CN structure to -0.719 eV for modified O-ACN-Ba structure). This outcome is also consistent with the observation of Ba-NO₈⁽⁺⁾ on O-ACN-Ba (Fig. 3a). Therefore, the present results indicate that the fabrication of O-ACN-Ba promotes the adsorption and activation of NO and subsequently furthers photocatalytic oxidation and conversion efficiency to suppress the production of the toxic intermediate NO₂, as evidenced by the *in situ* DRIFTS spectroscopy.

The photocatalytic NO oxidation is highly dependent on the ROS (superoxide radicals ·O₂⁻ and hydroxyl radicals ·OH), and thus the production of ·O₂⁻ was simulated using DFT by calculating the O₂ adsorption. In comparison with the bare CN (Fig. 4b), the O–O bond lengths in O-ACN-Ba are noticeably increased, resulting in weakened O–O Coulombic interactions. The adsorption energy of the O-ACN-Ba is increased significantly *via* more intense charge transfer between the O₂ and the O-ACN-Ba surface. Correspondingly, the O₂ molecules adsorbed on O-ACN-Ba are activated more easily and tend to receive more electrons for the production of ·O₂⁻ radicals to participate in the photocatalytic redox reaction—contributing to enhanced photocatalytic efficiency.

The enhanced generation of active radicals on O-ACN-Ba was also confirmed using the DMPO spin-trapping ESR experimental method. As expected, much stronger DMPO-·O₂⁻ signals were detected for O-ACN-Ba-030 than for pure CN (Fig. 4c). The increase in the signals associated with ·O₂⁻ radicals is linked directly to the improved adsorption and activation of O₂ molecules and expedited spatial charge separation, which enables O₂ molecules to be activated more easily for the generation of ·O₂⁻. In addition, increased signals characteristic for DMPO-·OH was also observed (Fig. 4d). The formation of ·OH can be traced back to the reduction of ·O₂⁻ in the sequence of ·O₂⁻ → H₂O₂ → ·OH, which demonstrates that the electron excitation and charge transportation on O-ACN-Ba-030 are effectively promoted.

The photocatalytic performance of the prepared samples towards

NO removal was evaluated under visible-light irradiation ($\lambda \geq 420$ nm). As shown in Fig. 4e, the O-ACN-Ba-030 sample exhibits a noticeably higher NO removal ratio than the pristine CN as a result of suppressed NO₂ production. The maximum NO removal ratio was observed after ca. 5 min. The visible-light irradiation could not cause the reduction of NO in the condition with no photocatalyst (Fig. S6). All O-ACN-Ba-X samples exhibited superior activity when compared to the pristine CN (Fig. 4e), which indicates that the photocatalytic efficiency of CN within the O-ACN-Ba structure is significantly enhanced. Also, to further demonstrate the interaction between CN and BaCO₃ during co-pyrolysis, the mechanically mixed CN-Ba sample is also tested, and a slight decrease of photocatalytic activity is observed. Thus, a facile co-pyrolysis method has been developed to prepare highly efficient CN within the O-ACN-Ba structure and the optimized preparation conditions are confirmed. As demonstrated by the combined experimental and theoretical approach, the designed O-ACN-Ba structure can boost the adsorption and activation of gas molecules (NO and O₂) participating in photocatalytic NO oxidation, and also expedite the spatial charge separation and thus promote the generation of ROS to optimize the photocatalytic efficiency. Overall, the results demonstrate that inhibited generation of toxic intermediate and accelerated transformation of NO have been realized, and then facilitate optimized photocatalytic oxidation, which is in accordance with the analysis of *in situ* DRIFTS.

3.4. Charge separation and transfer

The enhanced generation of ROS can increase the photocatalytic efficiency, mostly as a result of the enhanced adsorption and activation of gas molecules and efficient charge separation rate. Therefore, further experiments were carried out to probe the charge separation and charge transfer processes. Based on the quenching of PL peaks observed for O-ACN-Ba-030 sample (Fig. 5a) and the prolonged radiative lifetime of O-ACN-Ba-030 (Fig. 5b)—which increased from 2.64 ns (pristine CN) to 2.97 ns—it is apparent that the unique O-ACN-Ba structure can accelerate the separation of photogenerated charge carriers. Simultaneously, the stronger EPR signal intensity observed for O-ACN-Ba-030 reflects

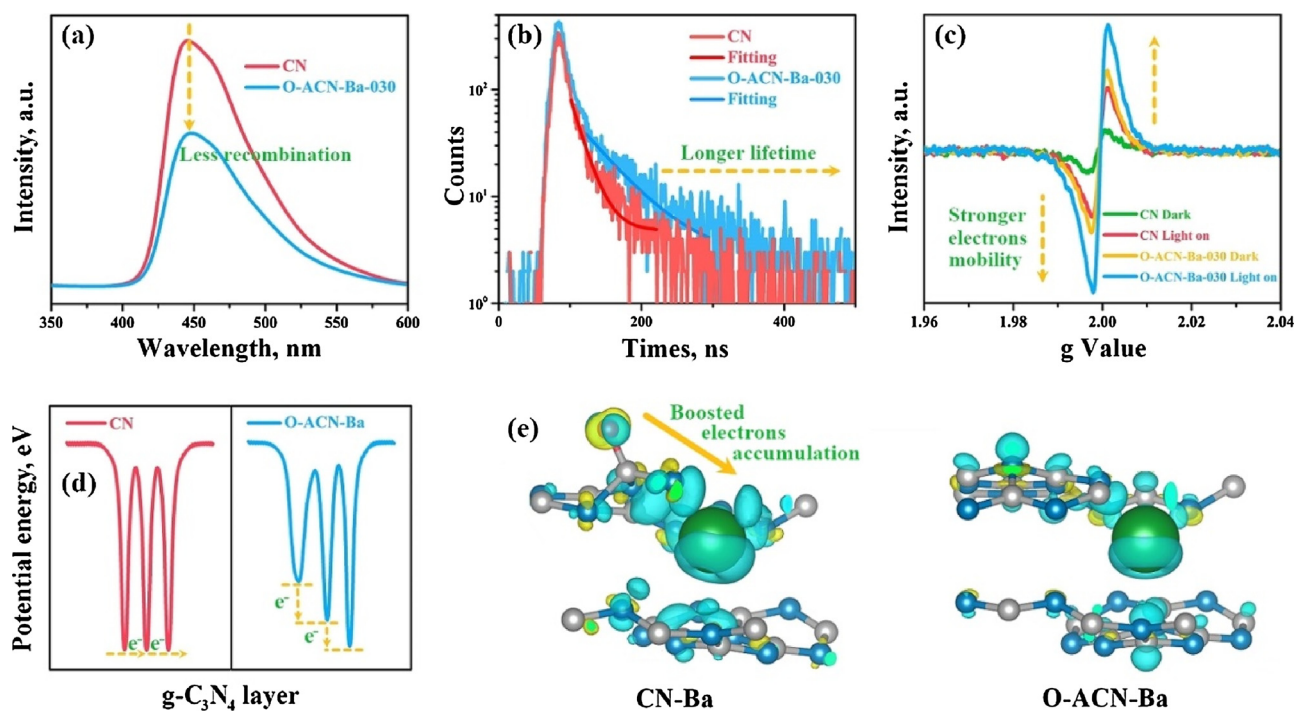


Fig. 5. Analysis of charge separation and charge transfer. Photoluminescence spectra (a), the ns-level time-resolved fluorescence spectra (b), and room temperature solid state EPR spectra (c) of CN and O-ACN-Ba-030; calculated electrostatic potential of CN and O-ACN-Ba (d); charge density difference distribution of pure CN and O-ACN-Ba (e): charge accumulation is shown in blue and depletion in yellow; gray, blue, green, red and pink spheres stand for C, N, Ba, O and H atoms, respectively; the isosurfaces are set to $0.005 \text{ eV } \text{\AA}^{-3}$ (For interpretation of the references to colour in this figure legend, the reader is referred to the web version of this article).

increased electron mobility and charge transportation (Fig. 5c).

In the next step, we investigated further electron transfer direction and pathway using DFT calculations. Fig. 5d reveals the energy barriers associated with transfer electrons between neighboring layers. The DFT calculations showed that the electrostatic potential of the second layer (L2) increased significantly after the introduction of O/Ba, which suggests that the barrier for electron transfer from L2 to L3 decreased. In addition, the electrostatic potential associated with L1 in O-ACN-Ba increased in comparison to that of pristine CN, which guarantees the vertical migration of electrons in the direction L1 → L2 → L3 in a one-way transmission manner, and promotes thus electron transfer with low recombination rate. As a consequence, the samples with O-ACN-Ba structure could extend the delocalized π bonds to deviate from the planes (i.e., the X and Y directions parallel to CN planes) and induce electron transfer toward the Z direction (i.e., the direction perpendicular to CN planes), thus accelerating the adsorption and activation of gas molecules and boosting the separation of charge carriers. In order to illustrate the gain or loss of electrons between the adjacent layers, we examined the differences in charge distribution of pure CN and O-ACN-Ba (Fig. 5e). The unique O-ACN-Ba structure allows redistribution of inner charge via the synergistic effects of ETS, ETA, and ETM. Specifically, intralayer-delocalized photogenerated electrons are converged and localized via the formation of ETS and introduction of ETA. Oriented interlayer-electron delivery channels are constructed by the introduction of ETM to further expedite the spatial charge separation. Therefore, the O-ACN-Ba structure permits increased electron localization and unprecedentedly high charge separation rate to be achieved to optimize the photocatalytic NO removal efficiency and suppress the production of toxic intermediate.

3.5. Optical properties and band structures

The light absorption properties of the prepared samples were investigated using a combined experimental and theoretical approach. As evidenced by UV-vis DRS spectroscopy, a red-shift in the optical

absorption band edge was observed for the O-ACN-Ba-030 sample (Fig. S8a, Experiment). In addition, the promoted light harvest was certified using the calculated absorption spectra (Fig. S8a, Calculation). Overall, the results suggested that the O/Ba co-functionalized amorphous carbon nitride could increase the density and distribution of localized states, broaden the absorption range in visible-light region, and narrow the band gap of CN for enhanced photocatalysis.

Finally, we calculated the total density of states (TDOS), and the results are shown in Fig. S8b. The band energy of pure CN was calculated to be 2.44 eV . As a result of the known limitations of plain DFT method, there is a tolerable error in the calculated value in comparison with the experimental one. The narrowing of the band gap of O/Ba co-functionalized amorphous carbon nitride indicates that it possesses enhanced visible-light absorption ability in comparison with pristine CN, and this outcome is consistent with the observations shown in Fig. S7a. Additionally, the valence band (VB) and conduction band (CB) edges of O-ACN-Ba were downshifted when compared to those of bare CN. Thus, it is apparent that the band structure of CN can be successfully tailored by co-functionalization with O and Ba. Specifically, within the O-ACN-Ba structure, the extra lone-pair electrons of the two-coordinated N atoms in CN are significantly localized by the introduction of local electronic trapping/converging districts and intralayer electronic mediators (ETS, ETA, and ETM), thus facilitating electron hopping from a higher energy level to a lower one. As a consequence, dramatically enhanced electron mobility, significantly increased light absorption ability, and effectively promoted oxidization ability of VB holes can be realized under visible-light illumination, affording a material with highly enhanced photocatalytic activity for NO removal.

4. Conclusions

The present work designs and develops an O/Ba co-functionalized amorphous carbon nitride (labeled as O-ACN-Ba) for the simultaneous optimization of photocatalytic NO removal efficiency and suppression of toxic intermediate generation. Also, the successful fabrication of O-

ACN-Ba, the photocatalytic NO conversion pathway underlying the reaction, and the promotion mechanisms in terms of enhanced photoelectric properties and photocatalytic efficiency are demonstrated by the highly combined experimental and theoretical methods. This research realizes the optimization photocatalytic NO removal, and provides a new method to advance the development of photocatalytic technology for efficient and safe air purification.

Acknowledgements

This work was supported by the National Natural Science Foundation of China (Grant Nos. 51478070, 21501016, and 21777011), the National Key R&D project (Grant No. 2016YFC0204702), and the Innovative Research Team of Chongqing (Grant No. CXTDG201602014), the Natural Science Foundation of Chongqing (Grant No. cstc2017jcyjBX0052) and the Plan for “National Youth Talents” of the Organization Department of the Central Committee. The authors also acknowledge the AM-HPC in Suzhou, China for computational support.

Appendix A. Supplementary data

Supplementary material related to this article can be found, in the online version, at doi:<https://doi.org/10.1016/j.apcatb.2018.06.071>.

References

- [1] J. Baxter, Z. Bian, G. Chen, D. Danielson, M.S. Dresselhaus, A.G. Fedorov, T.S. Fisher, C.W. Jones, E. Maginn, U. Kortshagen, Nanoscale design to enable the revolution in renewable energy, *Energy Environ. Sci.* 2 (2009) 559–588.
- [2] H. Wang, W. He, X. Dong, H. Wang, F. Dong, In situ FT-IR investigation on the reaction mechanism of visible light photocatalytic NO oxidation with defective g-C₃N₄, *Sci. Bull.* 63 (2018) 117–125.
- [3] X. Zhang, M. Fevre, G.O. Jones, R.M. Waymouth, Catalysis as an enabling science for sustainable polymers, *Chem. Rev.* 118 (2017) 839–885.
- [4] T. Hibino, K. Kobayashi, M. Ito, M. Nagao, M. Fukui, S. Teranishi, Direct electrolysis of waste newspaper for sustainable hydrogen production: an oxygen-functionalized porous carbon anode, *Appl. Catal. B-Environ.* 231 (2018) 191–199.
- [5] P. Chen, F. Dong, M. Ran, J. Li, Synergistic photo-thermal catalytic NO purification on MnO_x/g-C₃N₄: enhanced performance and reaction mechanism, *Chin. J. Catal.* 39 (2018) 619–629.
- [6] J. West, A. Cohen, F. Dentener, B. Brunekreef, T. Zhu, B. Armstrong, M. Bell, M. Brauer, G.R. Carmichael, D. Costa, What we breathe impacts our health: improving understanding of the link between air pollution and health, *Environ. Sci. Technol.* 50 (2016) 4895–4904.
- [7] H.X. Li, Z.F. Bian, J. Zhu, Y.N. Huo, H. Li, Y.F. Lu, Mesoporous Au/TiO₂ nanocomposites with enhanced photocatalytic activity, *J. Am. Chem. Soc.* 129 (2007) 4538–4539.
- [8] J. Kim, D. Monllorsatoca, W. Choi, Simultaneous production of hydrogen with the degradation of organic pollutants using TiO₂ photocatalyst modified with dual surface components, *Energy Environ. Sci.* 5 (2012) 7647–7656.
- [9] X. Dong, J. Li, Q. Xing, Y. Zhou, H. Huang, F. Dong, The activation of reactants and intermediates promotes the selective photocatalytic NO conversion on electron-localized Sr-intercalated g-C₃N₄, *Appl. Catal. B-Environ.* 232 (2018) 69–76.
- [10] C. Xu, H. Liu, D. Li, J.H. Su, H.L. Jiang, Direct evidence of charge separation in a metal–organic framework: efficient and selective photocatalytic oxidative coupling of amines via charge and energy transfer, *Chem. Sci.* 9 (2018) 3152–3158.
- [11] T. Hisatomi, J. Kubota, K. Domen, ChemInform abstract: recent advances in semiconductors for photocatalytic and photoelectrochemical water splitting, *Chem. Soc. Rev.* 43 (2014) 7520.
- [12] M.N. Lyulyukin, P.A. Kolinko, D.S. Selishchev, D.V. Kozlov, Hygienic aspects of TiO₂-mediated photocatalytic oxidation of volatile organic compounds: air purification analysis using a total hazard index, *Appl. Catal. B-Environ.* 220 (2017) 386–396.
- [13] S. Weon, W. Choi, TiO₂ nanotubes with open channels as deactivation-resistant photocatalyst for the degradation of volatile organic compounds, *Environ. Sci. Technol.* 50 (2016) 2556.
- [14] H. Wang, Y. Sun, G. Jiang, Y. Zhang, H. Huang, Z. Wu, S.C. Lee, F. Dong, Unraveling the mechanisms of visible light photocatalytic NO purification on earth-abundant insulator-based core-shell heterojunctions, *Environ. Sci. Technol.* 52 (2018) 1479–1487.
- [15] Z. Wang, Y. Huang, L. Chen, M. Chen, J. Cao, W.K. Ho, S.C. Lee, In-situ g-C₃N₄ self-sacrificial synthesis of g-C₃N₄/LaCO₃OH heterostructure with booming interfacial charge transfer and separation for photocatalytic NO removal, *J. Mater. Chem. A* 6 (2017) 972.
- [16] W. Cui, J. Li, F. Dong, Y. Sun, G. Jiang, W. Cen, S.C. Lee, Z. Wu, Highly efficient performance and conversion pathway of photocatalytic NO oxidation on SrO-clusters@amorphous carbon nitride, *Environ. Sci. Technol.* 51 (2017) 10682.
- [17] I. Papailias, N. Todorova, T. Giannakopoulou, S. Karapati, N. Boukos, D. Dimotikali, C. Trapalis, Enhanced NO_x abatement by alkaline-earth modified g-C₃N₄ nanocomposites for efficient air purification, *Appl. Surf. Sci.* 430 (2017) 225–233.
- [18] H. Wang, W. Zhang, X. Li, J. Li, W. Cen, Q. Li, F. Dong, Highly enhanced visible light photocatalysis and in situ FT-IR studies on Bi metal@defective BiOCl hierarchical microspheres, *Appl. Catal. B-Environ.* 225 (2018) 218–227.
- [19] P. Zhang, T. Wang, X. Chang, J. Gong, Effective charge carrier utilization in photocatalytic conversions, *Acc. Chem. Res.* 49 (2016) 911.
- [20] H. Zhu, N. Goswami, Q. Yao, T. Chen, Y. Liu, Q. Xu, D. Chen, J.M. Lu, J. Xie, Cyclodextrin-gold nanoclusters on TiO₂ enhances photocatalytic decomposition of organic pollutants, *J. Mater. Chem. A* 6 (2017) 1102–1108.
- [21] W. Cui, J. Li, W. Cen, Y. Sun, S.C. Lee, F. Dong, Steering the interlayer energy barrier and charge flow via bioriented transportation channels in g-C₃N₄: enhanced photocatalysis and reaction mechanism, *J. Catal.* 352 (2017) 351–360.
- [22] C.B. Anders, J.E. Eixenberger, N.A. Franco, R.J. Hermann, K.D. Rainey, J.J. Chess, A. Punnoose, D.G. Wingett, ZnO nanoparticle preparation route influences surface reactivity, dissolution and cytotoxicity, *Environ. Sci. Nano* 5 (2018) 572–588.
- [23] H. Tong, S. Ouyang, Y. Bi, N. Umezawa, M. Oshikiri, J. Ye, Nano-photocatalytic materials: possibilities and challenges, *Adv. Mater.* 24 (2012) 229.
- [24] Y.L. Li, P.P. Li, J.S. Wang, Y.L. Yang, W.Q. Yao, Z. Wei, J.S. Wu, X.X. Yan, X.F. Xu, Y.H. Liu, Y.F. Zhu, Water soluble graphitic carbon nitride with tunable fluorescence for boosting broad-response photocatalysis, *Appl. Catal. B-Environ.* 255 (2018) 519–529.
- [25] W.J. Ong, L.L. Tan, Y.H. Ng, S.T. Yong, S.P. Chai, Graphitic carbon nitride (g-C₃N₄)-based photocatalysts for artificial photosynthesis and environmental remediation: are we a step closer to achieving sustainability? *Chem. Rev.* 116 (2016) 7159.
- [26] X. Wang, K. Maeda, A. Thomas, K. Takanabe, G. Xin, J.M. Carlsson, K. Domen, M. Antonietti, A metal-free polymeric photocatalyst for hydrogen production from water under visible light, *Nat. Mater.* 8 (2009) 76–80.
- [27] X. Wang, S. Blechert, M. Antonietti, Polymeric graphitic carbon nitride for heterogeneous photocatalysis, *ACS Catal.* 2 (2012) 1596–1606.
- [28] K. Maeda, X. Wang, Y. Nishihara, Photocatalytic activities of graphitic carbon nitride powder for water reduction and oxidation under visible light, *J. Phys. Chem. C* 113 (2009) 4940–4947.
- [29] F. Dong, Z. Zhao, T. Xiong, Z. Ni, W. Zhang, Y. Sun, W.K. Ho, *In situ* construction of g-C₃N₄/g-C₃N₄ metal-free heterojunction for enhanced visible-light photocatalysis, *ACS Appl. Mater. Interfaces* 5 (2013) 11392–11401.
- [30] L.B. Jiang, X.Z. Yuan, Y. Pan, J. Liang, Z.B. Wu, H. Wang, Doping of graphitic carbon nitride for photocatalysis: a review, *Appl. Catal. B-Environ.* 217 (2017) 388–406.
- [31] S. Panneri, P. Ganguly, B.N. Nair, A.M. Peer, K.G.K. Warrier, Co₃O₄-C₃N₄ p-n nanoheterojunctions for the simultaneous degradation of a mixture of pollutants under solar irradiation, *Environ. Sci. Nano* 4 (2017) 212–221.
- [32] G. Zhang, M. Zhang, X. Ye, X. Qiu, S. Lin, X. Wang, Iodine modified carbon nitride semiconductors as visible light photocatalysts for hydrogen evolution, *Adv. Mater.* 26 (2014) 805.
- [33] Y. Kang, Y. Yang, L.C. Yin, X. Kang, L. Wang, G. Liu, H.M. Cheng, Selective breaking of hydrogen bonds of layered carbon nitride for visible light photocatalysis, *Adv. Mater.* 28 (2016) 6471–6477.
- [34] H. Yu, R. Shi, Y. Zhao, T. Bian, Y. Zhao, C. Zhou, G.I. Waterhouse, L.Z. Wu, C.H. Tung, T. Zhang, Alkali-assisted synthesis of nitrogen deficient graphitic carbon nitride with tunable band structures for efficient visible-light-driven hydrogen evolution, *Adv. Mater.* 29 (2017) 5148.
- [35] H. Gao, S. Yan, J. Wang, Y.A. Huang, P. Wang, Z. Li, Z. Zou, Towards efficient solar hydrogen production by intercalated carbon nitride photocatalyst, *Phys. Chem. Chem. Phys.* 15 (2013) 18077–18084.
- [36] T. Xiong, W. Cen, Y. Zhang, F. Dong, Bridging the g-C₃N₄ interlayers for enhanced photocatalysis, *ACS Catal.* 6 (2016) 2462–2472.
- [37] J. Li, W. Cui, Y. Sun, Y. Chu, W. Cen, F. Dong, Directional electrons delivery via vertical channel between g-C₃N₄ layers promoting the photocatalysis efficiency, *J. Mater. Chem. A* 5 (2017) 9358–9364.
- [38] G. Kresse, J. Furthmüller, Efficient iterative schemes for ab initio total-energy calculations using a plane-wave basis set, *Phys. Rev. B* 54 (1996) 11169–11186.
- [39] J.P. Perdew, K. Burke, M. Ernzerhof, Generalized gradient approximation made simple, *Phys. Rev. Lett.* 77 (1996) 3865–3868.
- [40] P.E. Blochl, Projector augmented-wave method, *Phys. Rev. B* 50 (1994) 17953–17979.
- [41] G. Kresse, D. Joubert, From ultrasoft pseudopotentials to the projector augmented-wave method, *Phys. Rev. B* 59 (1999) 1758–1775.
- [42] M.E. Tuckerman, Ab initio molecular dynamics: basic concepts, current trends and novel applications, *J. Phys. Condens. Matter* 14 (2002) R1297.
- [43] M. Born, W. Heisenberg, Zur Quantentheorie der Moleküle, *Ann. Phys.* 379 (1927) 1–31.
- [44] R. Bader, *Atoms in Molecules: a Quantum Theory*, Oxford University Press, 1994.
- [45] G. Zhang, J. Zhang, M. Zhang, X. Wang, Polycondensation of thiourea into carbon nitride semiconductors as visible light photocatalysts, *J. Mater. Chem.* 22 (2012) 8083–8091.
- [46] B.V. Lotsch, M. Döblinger, J. Sehnert, L. Seyfarth, J. Senker, O. Oeckler, W. Schnick, Unmasking melon by a complementary approach employing electron diffraction, solid-state NMR spectroscopy, and theoretical calculations-structural characterization of a carbon nitride polymer, *Chem. Eur. J.* 13 (2007) 4969–4980.
- [47] J. Zhang, G. Zhang, X. Chen, S. Lin, L. Möhlmann, G. Dolega, G. Lipner, M. Antonietti, S. Blechert, X. Wang, Co-monomer control of carbon nitride semiconductors to optimize hydrogen evolution with visible light, *Angew. Chem. Int. Ed.* 124 (2012) 3237–3241.

[48] F. Dong, Z. Wang, Y. Li, W.K. Ho, S.C. Lee, Immobilization of polymeric g-C₃N₄ on structured ceramic foam for efficient visible light photocatalytic air purification with real indoor illumination, *Environ. Sci. Technol.* 48 (2014) 10345–10353.

[49] Z.F. Huang, J. Song, L. Pan, Z. Wang, X. Zhang, J.J. Zou, W. Mi, X. Zhang, L. Wang, Carbon nitride with simultaneous porous network and O-doping for efficient solar-energy-driven hydrogen evolution, *Nano Energy* 12 (2015) 646–656.

[50] F. Lin, Z. Wang, Q. Ma, Y. Yang, R. Whiddon, Y. Zhu, K. Cen, Catalytic deep oxidation of NO by ozone over MnO_x loaded spherical alumina catalyst, *Appl. Catal. B-Environ.* 198 (2016) 100–111.

[51] Y. Lin, D. Su, Fabrication of nitrogen-modified annealed nanodiamond with improved catalytic activity, *ACS Nano* 8 (2014) 7823–7833.

[52] J. Li, Y. Shi, D. Fan, W. Cen, Y. Chu, Tailoring active sites via synergy between graphitic and pyridinic N for enhanced catalytic efficiency of a carbocatalyst, *ACS Appl. Mater. Interfaces* 9 (2017) 19861–19869.

[53] T. Weingand, S. Kuba, K. Hadjiivanov, H. Knözinger, Nature and reactivity of the surface species formed after NO adsorption and NO + O₂ coadsorption on a WO₃–ZrO₂ catalyst, *J. Catal.* 209 (2002) 539–546.

[54] L. Zhong, Y. Yu, W. Cai, X. Geng, Q. Zhong, Structure-activity relationship of Cr/Ti-PILC catalysts using a pre-modification method for NO oxidation and their surface species study, *Phys. Chem. Chem. Phys.* 17 (2015) 15036–15045.

[55] K.I. Hadjiivanov, Identification of neutral and charged NxOy surface species by IR spectroscopy, *Catal. Rev.* 42 (2007) 71–144.